The Cryosphere

Open Access

EGU

Supplement of

Snow stratigraphy observations from Operation IceBridge surveys in Alaska using S and C band airborne ultra-wideband FMCW (frequency-modulated continuous wave) radar

Jilu Li et al.

Correspondence to: Jilu Li (jiluli@ku.edu.com)

Supplementary sections

S1: The radar system's impulse response and data deconvolution
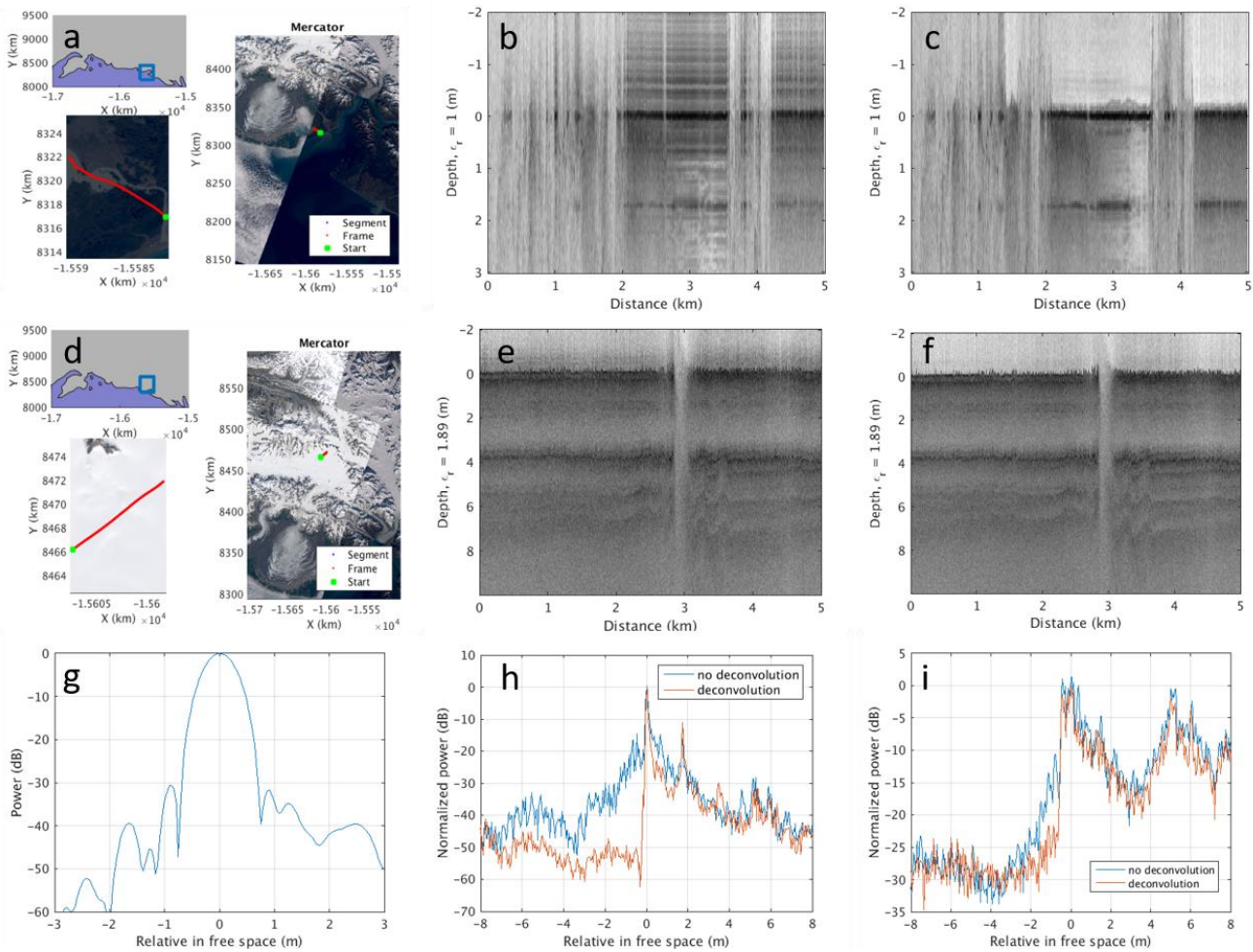
Figure S1: Radar's system impulse response and sample result of deconvolution. (a) The flight line over Malaspina Lake on the Landsat image map; (b) The radar echogram from the lake reflections showing the sidelobes; (c) The radar echogram from the lake reflections after deconvolution; (d) The flight line over Seaward Glacier on the Landsat image map; (e) The radar echogram of Seaward Glacier showing sidelobes; (f) The radar echogram of Seaward Glacier after deconvolution; (g) The radar's system impulse response derived from lake surface reflections in (a); (h) A-scopes from (b) and (c) showing sidelobe reductions after deconvolution; (i) A-scopes from (e) and (f) showing sidelobe reductions after deconvolution.

As shown in Fig. S1(a), we flew over Malaspina Lake along the grid lines for Malaspina Glacier survey on May 5th, 2021. We used the reflections from the lake to derive the radar's impulse response (Fig. S1(g)). Figure S1 (b) and Fig. S1(c) compare the echograms from the lake surface reflections before and after the deconvolution using the derived radar's impulse response in Fig. S1(g). Figure S1(d) shows the flight line for the Seaward Glacier survey on May 2rd, 2021. Figure S1(e) and Fig. S1(f)

compare the echograms from Seaward Glacier before and after the deconvolution using the derived radar's impulse response of (g). Fig. S1(h) and (i) compare the A-scopes showing the sidelobe reductions after deconvolution. In Fig. S1(a) and Fig. S1 (d), the red segments in the left maps are zoom-in versions of the right maps showing the data frame locations of the radar echograms of (b) and (e), and the green dot marks the starting point.

20

S2: Additional example of snow accumulation layers observed at Bona-Churchill summit areas

We provide an additional example radar echogram in this supplementary section. As shown in Fig. S2(a), the deepest snow accumulation layer observed by the radar is at the depth of ~128 m as annotated by the black arrow, assuming a value of 2.96 for the relative snow permittivity in the depth calculation. We collected this data along the red line as shown on the map in

25 Fig. S2(b). This location is also marked by the blue circle on the map in Fig. 3(b).
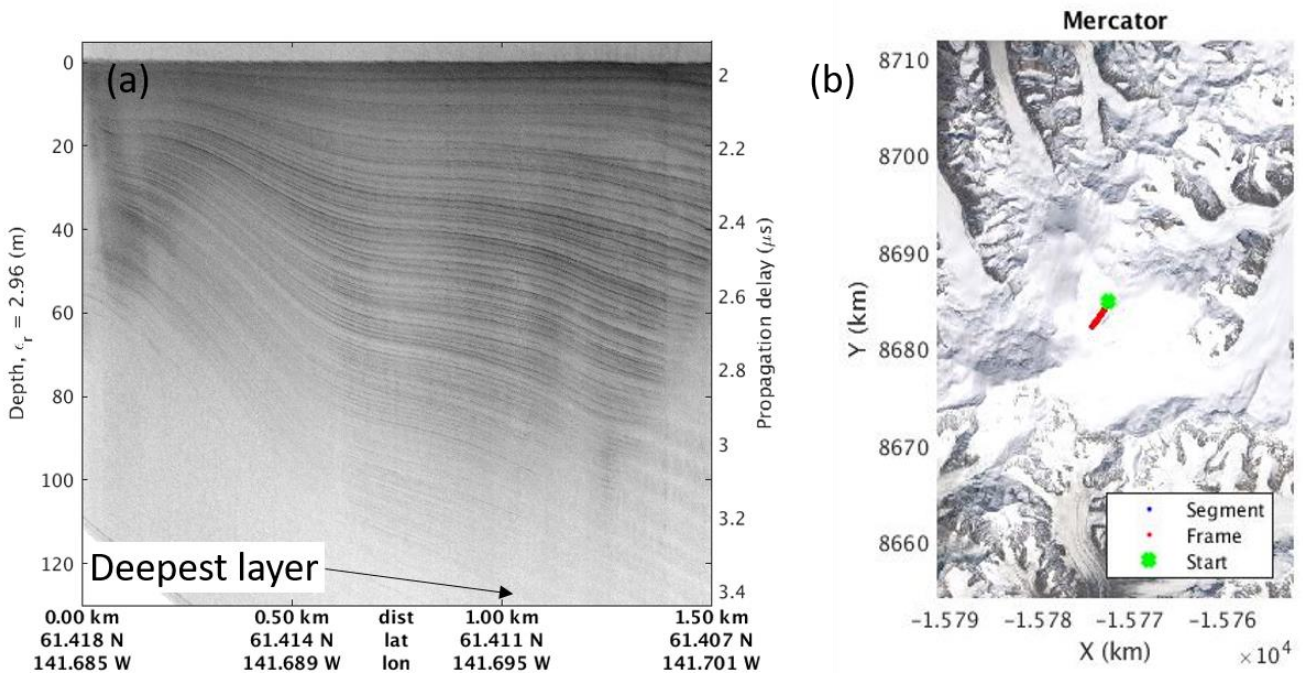
Figure S2: (a) Dense snow accumulation layers observed near Mount Churchill; (b) The flight line (in red) on the Landsat image map.

30

S3: Snow surface elevation comparisons along repeated flight lines of 2018 and 2021 over Mount Wrangell caldera
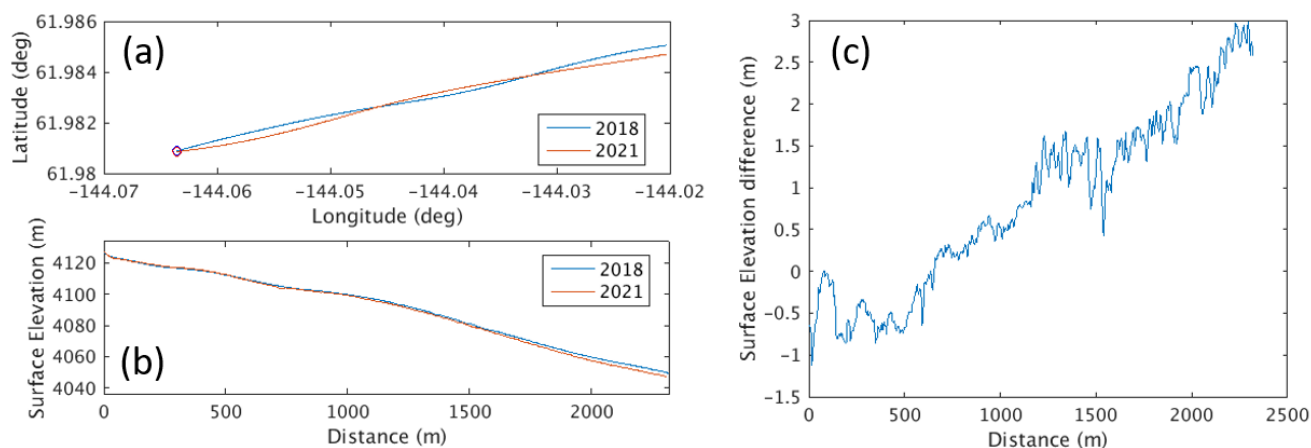
Figure S3: (a) Repeated flight paths of 2018(orange) and 2021(blue), in which the circles mark the start points, and the offsets between the two paths are within 40 m; (b) Surface elevations from the snow radar measurements after constant offset calibrations (-2.89 m and -3.12 m respectively for 2018 and 2021) using coincidental laser measurements, and the slope of the surface is less than 2 degrees; (c) Surface elevation differences between 2018 and 2021, and a positive values means the surface elevation of 2018 is higher.

S4: Detailed surface mass balance (SMB) analysis using Modèle Atmosphérique Régional (MAR) model

According to the MAR data, Table S4 gives the mean, standard deviation, the slope of linear fitting and the changes based on the fitted linear trend for the SMB, snowfall, rainfall, melt, runoff, surface temperature, and snow densities in the first 10 m depths between 2003 and 2021. We concluded that the increasing accumulation over this period was associated with the increase in snowfall and rainfall events due to global warming and was primarily balanced by an increase in densification rate, with flow divergence playing a smaller role. As shown in the table and Fig. 9 (d), the snow surface temperature at the study site increased 0.86 °C. The snowfall and rainfall contributed about 88% and 12% to the SMB increase, respectively. There might be some melt in summer. There were no runoffs, which means the melt did not contribute to SMB and the rainfall was fully retained by snowpacks. Sublimation/evaporation was small and constant over 2003-2021.

Table S4: SMB process at the 2004 ice core/2005 temperature sensor tower site between 2003-2021

	SMB (m w.e.a^{-1})	Snowfall (m w.e. a^{-1})	Rainfall (m w.e.a^{-1})	Melt (m w.e. a^{-1})	Density (0-10m) (kg/m^3)	Temperature (°C)
mean	2.96	2.97	0.0078	0.0516	410.2	-15.8
std dev	0.26	0.27	0.0236	0.0556	26.8	1.0
slope (a^{-1})	0.012	0.011	0.0016	0.0005	1.8	0.051
change	0.205	0.180	0.0270	0.0087	21.7	0.86

Figure S4 shows the densification rate at the 2004 ice core/2005 temperature sensor tower site computed using the interpretation models. According to this figure, most part of the densification process happened in the first 1.5 years within the

first 10 m depths. 10 m is the depth where the critical pressure is reached. According to MAR, the SMB was 2.65 m. w. e., and the mean snow density for the 0-10 m in 2021 was 417.2 kg/m3. This means the SMB was equivalent to 6.25 m of snow, and

55 the first 9.38 meter of snow in 2021 would be totally replaced after 1.5 year. The increase of the snow density of the 0-10 m is nearly statistically significant, which is supportive evidence that the snowpacks absorbed the increased rainfall and melt. This also   explains why accumulation was increasing but not the surface elevation.
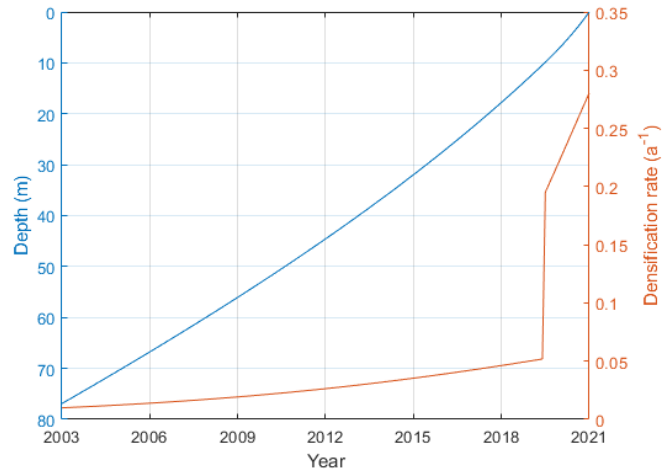
Figure S4: Depth and densification rate between 2003-2021 (tower site)

60

S5: Radar echograms contain the transition from wet snow facies to ice facies for multiple glaciers

All figures in this supplementary section are similar to Fig. 10 and we identified the snowline locations and elevations in Table 3 according to these figures. For detailed descriptions about these figures, see the discussions in the paper about Fig. 10. The caption of each figure here gives the snowline geolocations (longitude, latitude, elevation). The vertical red dashed line in each

65 radar echogram marks the snowline location. The average backscattering intensities in dB given in captions were computed from the left side and right side areas of the blue rectangular box split by vertical red dashed lines in the radar echograms. The higher average backscattering corresponds to wet-snow facies and lower to ice facies.
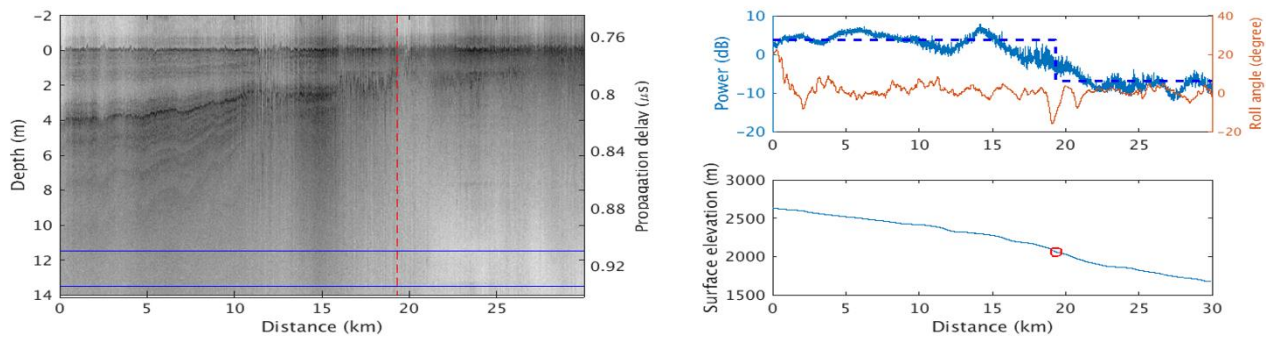
Figure S5-1: Glacier Kaskawulsh. The snowline is at 19.32 km (60.7501N, 139.3066W, 2062.00 m); backscattering in

70 **rectangular box (3.73dB, -6.89dB); CReSIS data frames: 20210510_03_001-006.**

4
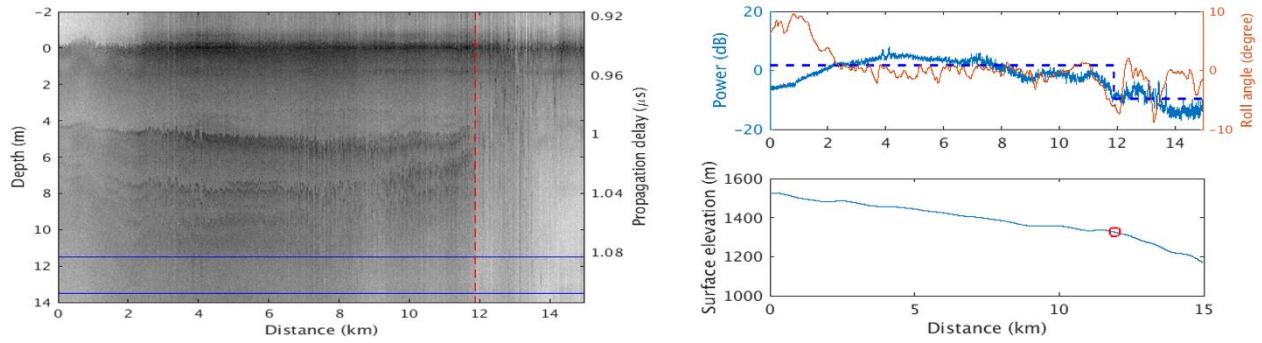
Figure S5-2: Glacier Steller. The Snowline is at 11.89 km (60.5913N, 143.4026W, 1325.90 m); backscattering in rectangular box (1.71dB, -9.59dB); CReSIS data frames: 20210512_02_003-005.
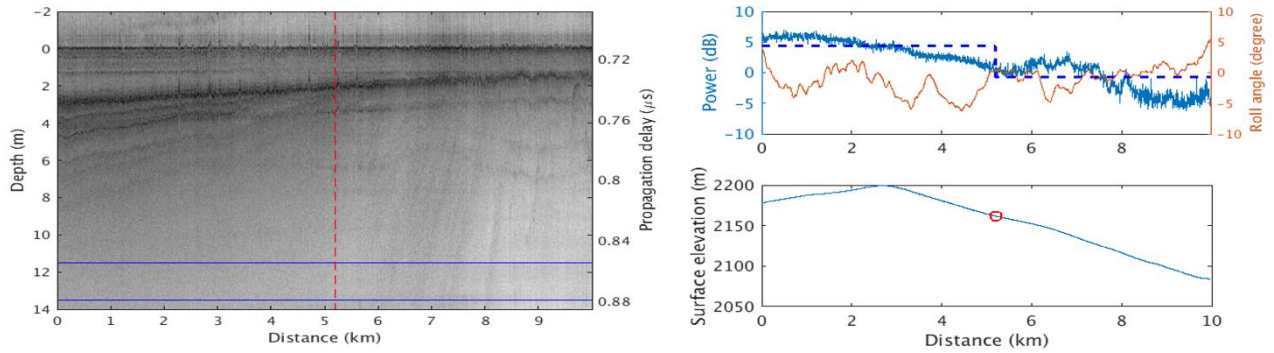
75 **Figure S5-3: Glacier Logan. The snowline is at 5.194 km (60.7215N, 140.1521W, 2161.84 m); backscattering in rectangular box (4.35dB, -0.67dB); CReSIS data frames: 20210512_02_003-005.**
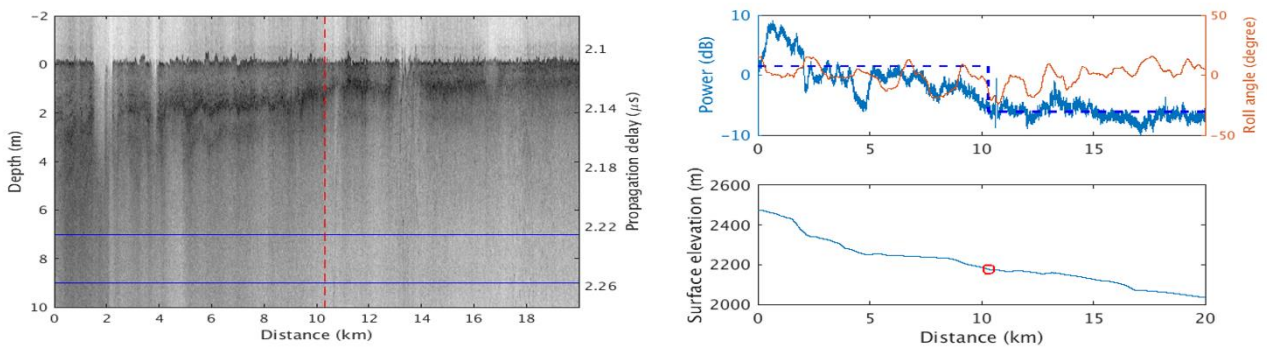
Figure S5-4: Glacier Nabesna. The snowline is at 10.310 km (61.8658N, 143.4937W, 2176.01 m); backscattering in rectangular box (1.49dB, -6.13dB); CReSIS data frames: 20210503_03_015-018.

80

5
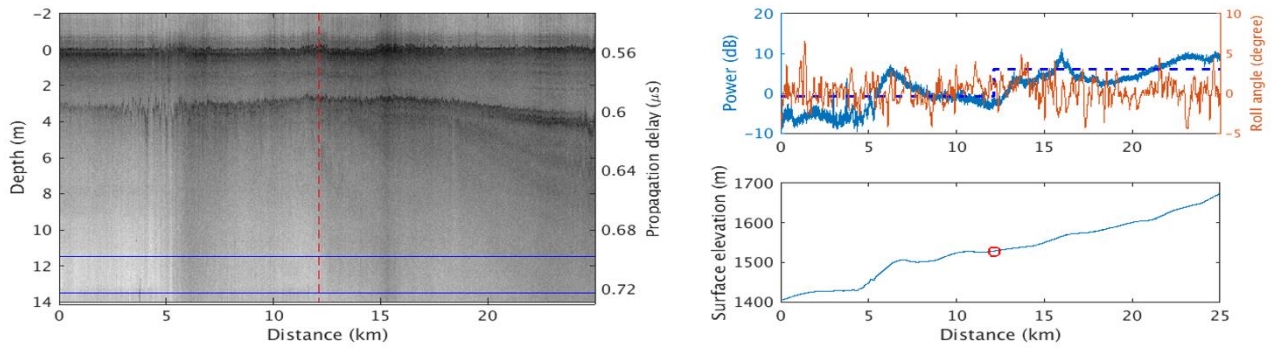
Figure S5-5: East Bagley Ice Field. The snowline is at 12.11 km (60.4967N, 141.7715W, 1528.14 m); backscattering in rectangular box (-0.75dB, 6.00dB); CReSIS data frames: 20210513_02_002-006.